ACS Energy LETTERS

Cite This: ACS Energy Lett. 2018, 3, 2816−2822

http://pubs.acs.org/journal/aelccp

LETTER

Unlocking Bifunctional Electrocatalytic Activity for CO_2 Reduction Reaction by Win-Win Metal−Oxide Cooperation

Zhao Cai,[†,#] Yueshen Wu,[#] Zishan Wu,[#] Lichang Yin,[*,‡] Zhe Weng,[#] Yiren Zhong,[#] Wenwen Xu,[†,#] Xiaoming Sun,[*,†,§] and Hailiang Wang[*,#]

[†]State Key Laboratory of Chemical Resource Engineering, Beijing Advanced Innovation Center for Soft Matter Science and Engineering, Beijing University of Chemical Technology, Beijing 100029, P.R. China

[#]Department of Chemistry and Energy Sciences Institute, Yale University, West Haven, Connecticut 06516, United States

[‡]Shenyang National Laboratory for Materials Science, Institute of Metal Research, Chinese Academy of Sciences, Shenyang 110016, P.R. China

[§]College of Energy, Beijing University of Chemical Technology, Beijing 100029, P.R. China

Supporting Information

ABSTRACT: Understanding how remarkable properties of materials emerge from complex interactions of their constituents and designing advanced material structures to render desired properties are grand challenges. Metal−oxide interactions are frequently utilized to improve catalytic properties but are often limited to situations where only one component is facilitated by the other. In this work, we demonstrate highly cooperative win-win metal−oxide interactions that enable unprecedented catalytic functionalities for electrochemical CO_2 reduction reactions. In a single SnO_x/Ag catalyst, the oxide promotes the metal in the CO production mode, and meanwhile the metal promotes the oxide in the HCOOH production mode, achieving potential-dependent bifunctional CO_2 conversion to fuels and chemicals with H_2 evolution suppressed in the entire potential window. Spectroscopic studies and computational simulations reveal that electron transfer from Ag to SnO_x and dual-site cooperative binding for reaction intermediates at the SnO_x/Ag interface are responsible for stabilizing the key intermediate in the CO pathway, changing the potential-limiting step in the HCOOH pathway, and increasing the kinetic barrier in the H_2 evolution pathway, together leading to highly synergistic CO_2 electroreduction.

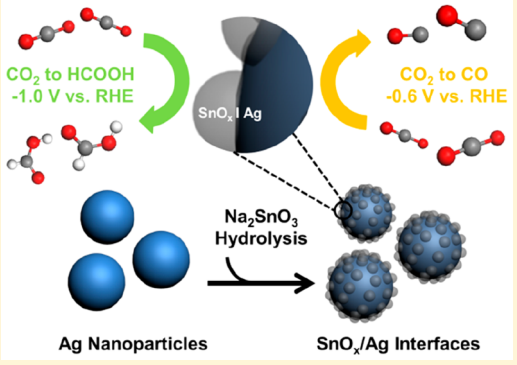

Driving energy-challenging chemical reactions in an efficient and sustainable way is essential toward solving current grand challenges and improving the quality of human life.[1−12] As a core area of research that may provide potential solutions, catalyst development has advanced to a stage in which multiple components are integrated in one catalyst structure to achieve more desirable properties. The catalytic performance, including selectivity, activity, and stability, of the principal active component is often promoted by the other constituents.[13−19] The increase in structural complexity poses scientific challenges in understanding the roles of the constituents and their interactions at the interfaces. Making use of multiple components and the electronic and chemical interactions between them within a catalyst structure to unlock unprecedented catalytic functionalities is scientifically intriguing and practically useful but remains highly challenging.

Strong metal−oxide interactions are widely adopted in the design of catalyst materials for thermochemical reactions in the gas phase, such as the Fischer−Tropsch synthesis,[20] water gas shift,[21] CO_2 hydrogenation to methanol,[22] and CO oxidation,[23] but have not been extensively utilized for electrocatalysis in the liquid phase.[24−26] In the field of electrochemical CO_2 reduction reactions, there have recently been several examples of enhanced catalysis based on metal/oxide hybrid material structures, including Co/Co_3O_4, Ag_xSn_y/SnO_z, and Cu/SnO_x for HCOOH production[27−30] and $Cu/In(OH)_3$, Au/CeO_x, and Cu/SnO_x for CO generation.[29−33] In all these examples, for a catalyst material with a specific structure and

Received: September 18, 2018
Accepted: October 19, 2018

DOI: 10.1021/acsenergylett.8b01767
ACS Energy Lett. 2018, 3, 2816−2822

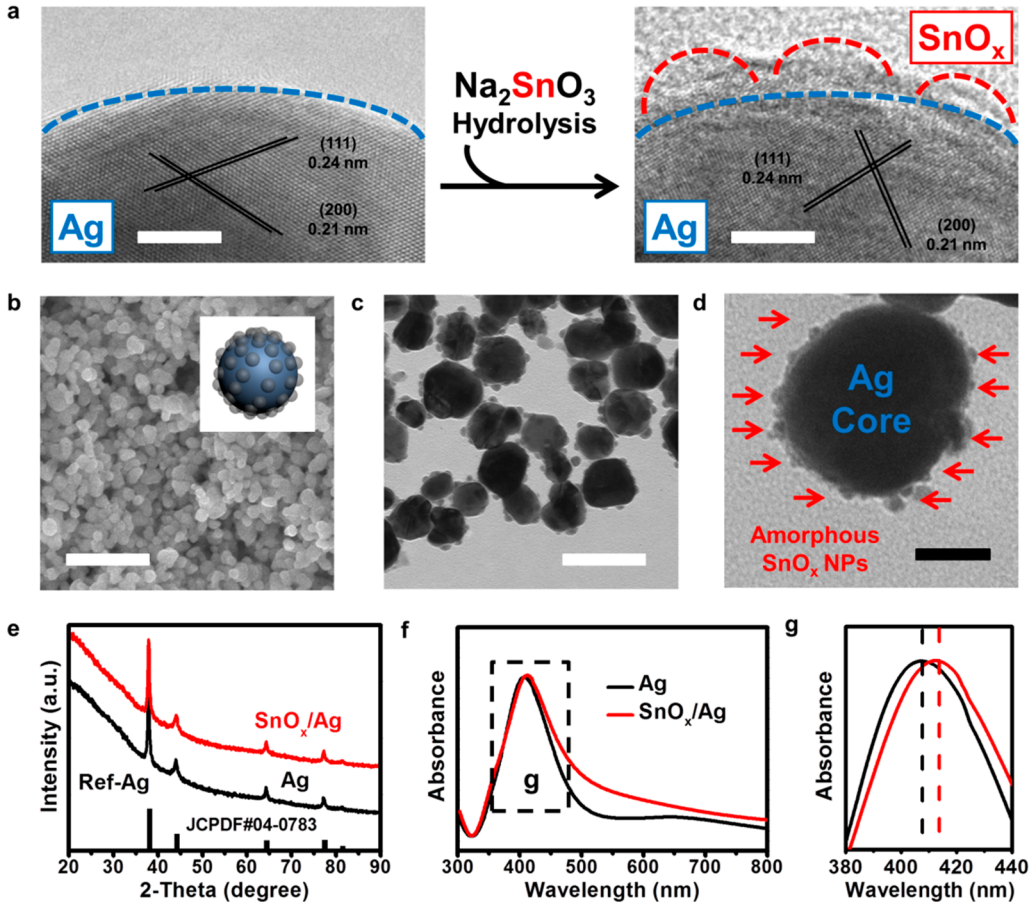

Figure 1. (a) High-resolution TEM images of Ag and SnO_x/Ag NPs. Scale bars: 5 nm. (b) Scanning electron microscopy (SEM) and (c) TEM images of SnO_x/Ag NPs. Scale bars: (b) 300 nm and (c) 100 nm. (d) Enlarged TEM image of a single SnO_x/Ag NP. Scale bar: 10 nm. (e) XRD patterns and (f) UV−vis spectra of Ag and SnO_x/Ag NPs. (g) Enlarged surface plasmon resonance area in the UV−vis spectra.

composition, there is only one type of catalytically active sites, and only one specific CO_2 electroreduction reaction is optimized.

In this work, we expand the scope of metal−oxide interactions in electrocatalysis by demonstrating a heterostructured SnO_x/Ag nanomaterial with unprecedented win-win metal−oxide cooperation and synergistic catalytic properties. In a single SnO_x/Ag catalyst material, the metal and oxide constituents, as controlled by the working electrode potential, can switch their roles of a major catalytic component and of a promoter, thus triggering two different CO_2 reduction reactions. In the more positive potential range (−0.6 to −0.8 V vs RHE), the oxide promotes the metal in converting CO_2 to CO, whereas in the more negative potential range (−0.8 to −1.1 V vs RHE), the metal facilitates the oxide in reducing CO_2 to HCOOH. The competing H_2 evolution reaction is effectively suppressed in this entire potential range. Because of the highly cooperative metal−oxide interactions, we successfully realize bifunctional electrocatalytic activity for CO_2 reduction, potential-controlled selective conversion to either CO or HCOOH, all based on one single catalyst. The origins of the metal−oxide cooperation are found via combined spectroscopic studies and theoretical calculations to be electron relocation at the metal/oxide interface and optimized binding for the key reaction intermediates at the metal−oxide dual sites.

The SnO_x/Ag catalyst material was synthesized with a two-step solution-phase method. Ag nanoparticles (NPs) with an average size of ∼30 nm were first prepared (Figure S1). Both high-resolution transmission electron microscopy (TEM) and X-ray diffraction (XRD) confirmed the crystalline nature of the Ag NPs (Figure 1a,e). SnO_x NPs with the size of ∼5 nm were then decorated on the surface of the Ag NPs via the hydrolysis reaction of Na_2SnO_3 to form the SnO_x/Ag heterostructure (Figure 1a−d). The resulting SnO_x was found to be amorphous (Figure 1a,e), which agrees well with similar SnO_x nanomaterials synthesized at low temperature.[30] Upon SnO_x attachment, the surface plasmon resonance peak of the Ag NPs moved from 407 to 413 nm, as recorded in the ultraviolet−visible (UV−vis) absorption spectra (Figure 1f, g). This red shift is because the SnO_x on the Ag NP surface has a higher refractive index (2.01) compared to the solvent water (1.33).[34,35] The atomic Ag/Sn ratio of the hybrid material is 88:12 (Table S1).

Catalytic properties of the SnO_x/Ag heteronanostructures for electrochemical CO_2 reduction were investigated in 0.5 M $KHCO_3$ aqueous solution and compared with both Ag and SnO_x NPs (Figure S2). Pure Ag NPs are able to reduce CO_2 to CO in the more negative potential range, with the highest Faradaic efficiency (FE) of 68% reached at −1.0 V vs RHE (Figure 2a−c). When the electrode potential is >−0.9 V, H_2 is the dominant product of electroreduction. No detectable HCOOH is generated in the entire potential range studied. The observed electrocatalytic behavior is consistent with what has been reported for typical Ag catalysts.[36] Pure SnO_x is also active for electrochemical CO_2 reduction, with HCOOH being

DOI: 10.1021/acsenergylett.8b01767
ACS Energy Lett. 2018, 3, 2816−2822

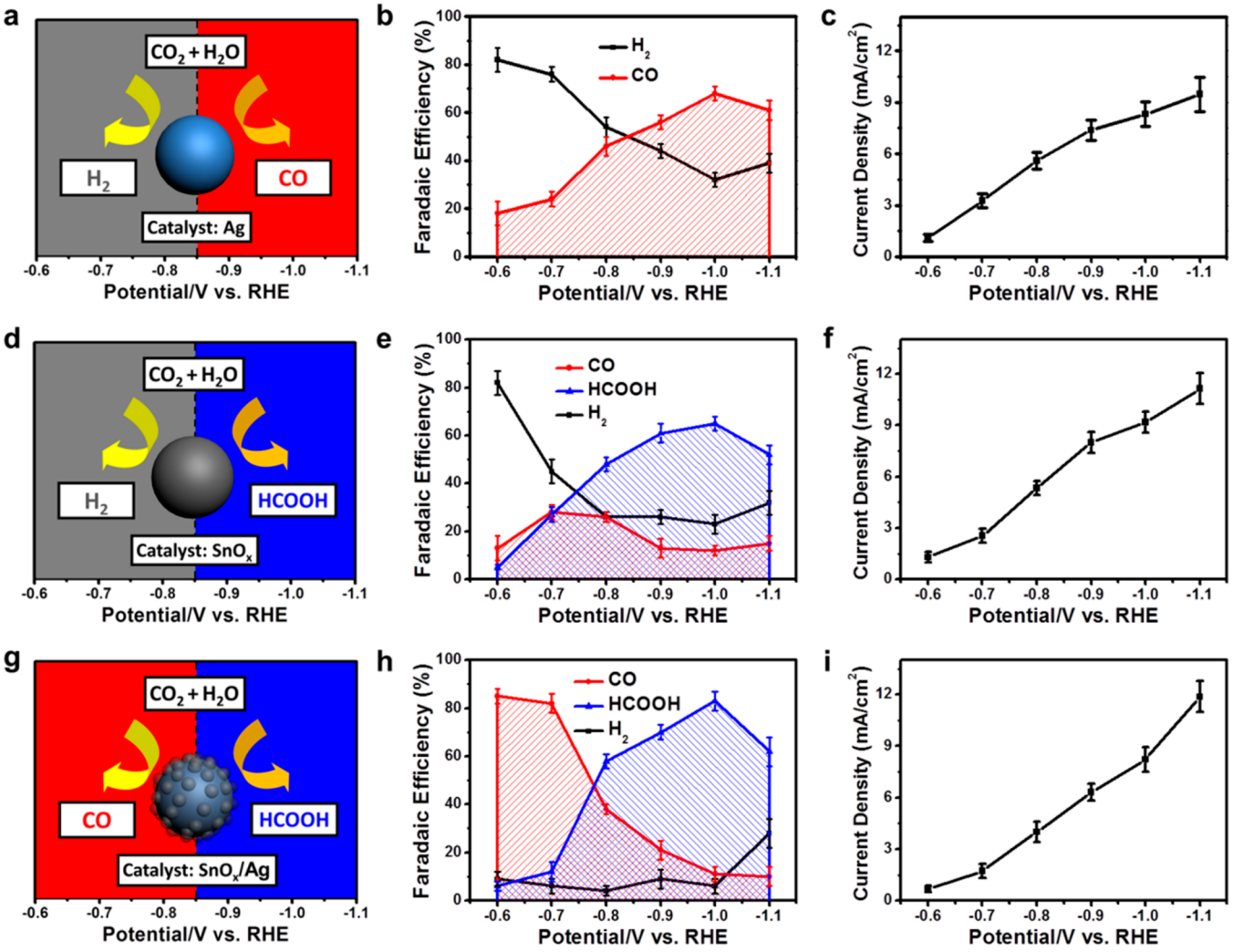

Figure 2. (a) Schematic illustration, (b) potential dependence of Faradaic efficiency of various products, and (c) total current density of CO_2 electroreduction catalyzed by Ag NPs in a 0.5 M $KHCO_3$ aqueous solution saturated with CO_2. The corresponding results for SnO_x and SnO_x/Ag are shown in panels d–f and g–i, respectively.

the major product in the potential range of −0.8 to −1.1 V (Figure 2d-f). The highest HCOOH FE is 65% at −1.0 V. At >−0.8 V, H_2 evolution is the major reaction. Throughout the entire potential range the CO FE remains lower than 28%. This performance is comparable to other SnO_x catalysts reported earlier.[28,37]

The SnO_x/Ag material, consisting of CO_2-to-CO active Ag and CO_2-to-HCOOH active SnO_x, possesses the catalytic functionalities of both components and, more remarkably, outperforms each constituent in their best aspect. The SnO_x/Ag hybrid catalyzes CO_2 electroreduction to CO in the more positive potential range (Figure 2g–i). The CO FE reaches 85% at −0.6 V vs RHE. Compared to pure Ag NPs, SnO_x/Ag exhibits much lower overpotential and improved FE in CO formation. The SnO_x/Ag hybrid catalyzes CO_2 electroreduction to HCOOH in the more negative potential range (Figure 2g–i). The HCOOH FE reaches 83% at −1.0 V. Compared to pure SnO_x, SnO_x/Ag shows significantly higher selectivity for HCOOH generation. Taken together, our SnO_x/Ag catalyst is able to selectively produce CO or HCOOH from CO_2 by adjusting the working electrode potential. In either mode, the catalyst retains good functional and structural durability after 12 h of continuous electrolysis (Figures S3 and S4). It is worth noting that within the entire working potential range from −0.6 to −1.0 V where bifunctional CO_2 conversion to CO and HCOOH is realized, the H_2 evolution reaction is suppressed to lower than 10% in FE.

When the SnO_x/Ag catalyst operates in the CO-producing mode, the Ag sites are mainly responsible for the catalysis and are enhanced by SnO_x to achieve lower overpotential and higher selectivity. When the HCOOH-producing mode is switched on, SnO_x becomes the major active sites and is promoted by Ag to reach higher catalytic selectivity. This hypothesis was verified as we systematically varied the amount of SnO_x deposited on the surface of Ag NPs in the synthesis. For pure Ag NPs without any SnO_x decoration, CO is the only CO_2 reduction product. In the SnO_x/Ag heterostructure, both the Ag and SnO_x sites are exposed on the surface (Figure 1c,d); thus, the catalyst is bifunctional. When we increase the amount of SnO_x by 8 times, the obtained Ag@SnO_x-400 material features a core–shell structure with the Ag surface completely covered by ∼3 nm of SnO_x (Figures S5–S8, Table S1). As a consequence, the selective CO production pathway is shut down and the catalyst exhibits SnO_x-like behavior (Figure S9). HCOOH is formed at −1.0 V vs RHE with a FE of 84%, which is higher than that on pure SnO_x because of the

DOI: 10.1021/acsenergylett.8b01767
ACS Energy Lett. 2018, 3, 2816–2822

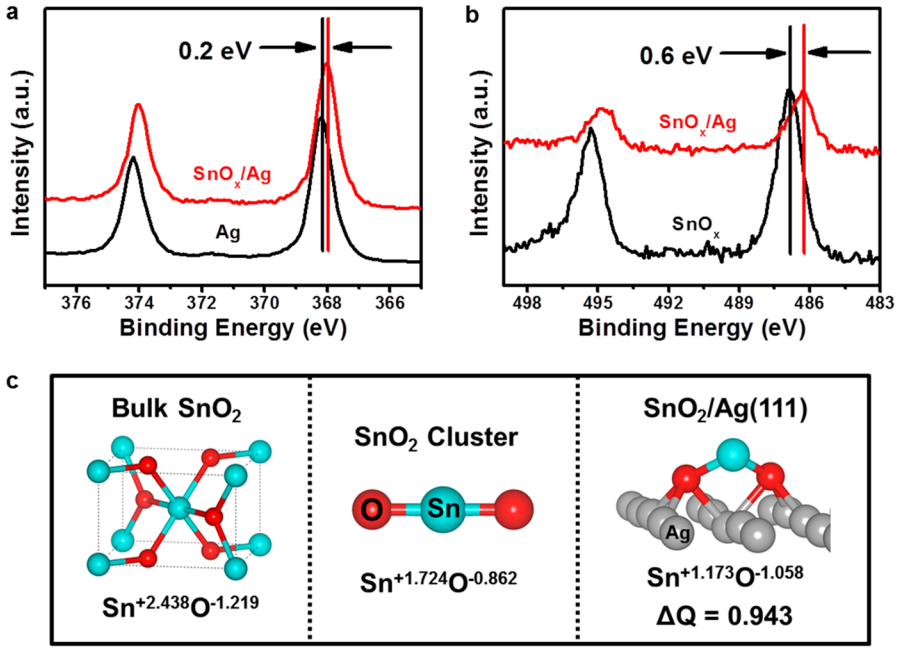

Figure 3. (a) Ag 3d and (b) Sn 3d XPS spectra for Ag, SnO_x, and SnO_x/Ag. (c) DFT simulation of electron transfer at the SnO_x/Ag interface.

enhancement by the Ag core.[38] When the amount of SnO_x is increased by 40 times, the resulting Ag@SnO_x-2000 material contains a thick layer of SnO_x wrapping the Ag NPs (Figure S10, Table S1), and the catalyst manifests selectivity and activity that are very similar to those of pure SnO_x (Figure S11).

The cooperation between metal and metal oxide enables the synergistic bifunctional electrocatalysis by our SnO_x/Ag hybrid material: in one mode of CO_2 reduction, SnO_x assists Ag in producing CO, whereas in the other mode Ag assists SnO_x in producing HCOOH. To the best of our knowledge, this is the first time that win-win metal−oxide interactions have been achieved for electrocatalysis. To date, Pd has been the only known material that can selectively convert CO_2 to HCOOH and CO at different potentials, but it is subject to serious deactivation due to CO contamination when operating in the HCOOH-producing mode.[39,40] Therefore, our SnO_x/Ag material also represents the first stable bifunctional catalyst for electrochemical CO_2 reduction reactions. The remarkable catalytic properties are a direct result of the strong metal−oxide interactions, which can be further broken down to (1) electronic interactions where the electronic structure of a catalyst surface and its binding strength for reaction intermediates are modified by electron relocation between metal and oxide and (2) interfacial cooperation which refers to metal−oxide dual sites affording more desirable adsorption geometry and energy for key reaction intermediates.

We first characterize the electronic interactions between the Ag and SnO_x components in the material structure by X-ray photoelectron spectroscopy (XPS). The binding energies of Ag 3d and Sn 3d electrons are recorded at 368.2/374.2 and 486.6/495.1 eV for pure Ag and SnO_x NPs (Figure 3a,b), characteristic of Ag(0) and Sn(IV) oxidation states, respectively. Upon formation of the SnO_x/Ag heterostructure, both the Ag 3d and Sn 3d XPS peaks shift to lower binding energy compared to the corresponding pure NPs (Figure 3a, b), indicating an increase in the oxidation state of Ag and a decrease for that of Sn.[28,41,42] We thus deduce that there is electron transfer from Ag to SnO_x in the hybrid structure. The dependence of the electron transfer on the amount of SnO_x coated on Ag is in full agreement with our deduction (Figure S12). As the amount of SnO_x increases, the Ag component becomes increasingly electron-deficient because there is more and more SnO_x withdrawing electrons, while the SnO_x becomes decreasingly electron-rich because there is more and more SnO_x sharing the electrons donated by Ag. The SnO_x/Ag catalyst was also characterized by quasi-in situ XPS measurements, the results of which suggest that both the Ag and Sn atoms maintain their oxidation states under the CO_2 electroreduction conditions (Figure S13). In addition, we prepared a physical mixture of Ag and SnO_x NPs, the XPS spectra of which show that there is electron relocation from Ag to SnO_x with a smaller magnitude compared to that for the SnO_x/Ag material (Figure S14). Accordingly, the physical mixture exhibits a bifunctional behavior with enhanced catalytic activity compared to the single components, but not as prominent as that of the SnO_x/Ag. The electron relocation in the SnO_x/Ag structure was simulated by density functional theory (DFT) calculations. A SnO_2 cluster on the Ag(111) surface (SnO_2/Ag(111)) was constructed to model the SnO_x/Ag interface (Figure 3c). Bader charge analysis reveals that the SnO_2 cluster draws electrons from the underlying Ag substrate. The net charge transfer from the Ag(111) substrate to the adsorbed SnO_2 cluster was calculated to be 0.943 electrons. This finding is in good consistency with the experimental XPS data.

We then analyze the energetics of CO_2 electroreduction to CO and HCOOH on the SnO_x/Ag surface. The pathway of CO_2 reduction to CO comprises three elementary steps (Figure 4a). On Ag(111), *COOH formation is the potential-limiting step (PLS) with an energy barrier of 0.91 eV, which matches well with previous reports.[29,43] Notably, the energy barrier of the potential-limiting *COOH formation step is reduced to 0.62 eV on the SnO_2/Ag(111) surface (Figure 4a), which explains the observed higher catalytic activity for CO_2-to-CO conversion. As for CO_2 reduction to HCOOH, we

DOI: 10.1021/acsenergylett.8b01767
ACS Energy Lett. 2018, 3, 2816−2822

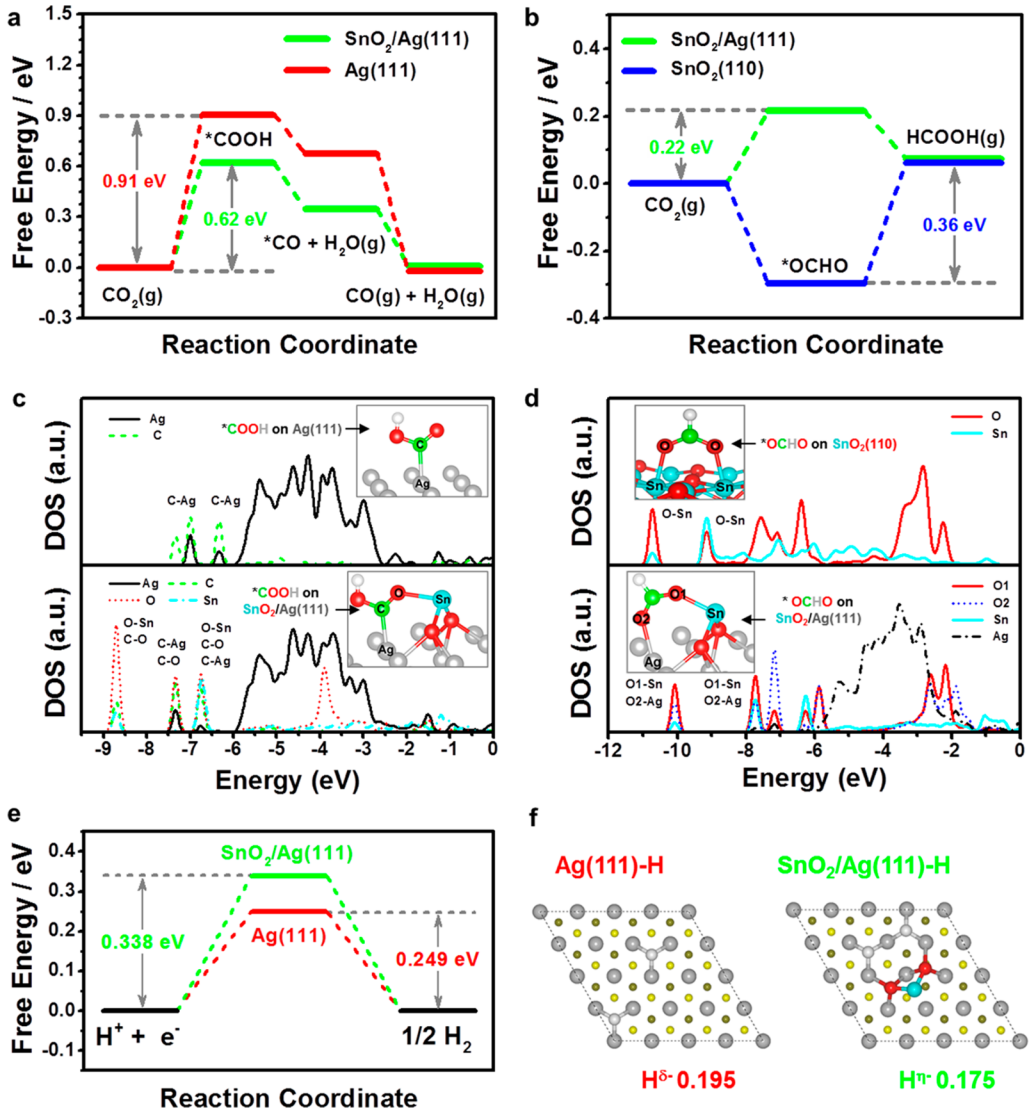

Figure 4. Free energy diagrams of (a) CO_2 reduction to CO on Ag(111) and SnO_2/Ag(111) and (b) CO_2 reduction to HCOOH on SnO_2(110) and SnO_2/Ag(111). DOS analysis of (c) *COOH on Ag(111) and SnO_2/Ag(111) and (d) *OCHO on SnO_2(110) and SnO_2/Ag(111), with the insets showing the optimized binding geometries. 0 eV corresponds to the Fermi level. (e) Calculated ΔG_{H^*} on Ag(111) and SnO_2/Ag(111). (f) Top views of the Ag(111) and SnO_2/Ag(111) surfaces with *H adsorbed.

compare the SnO_2/Ag(111) structure with the SnO_2(110) surface. The PLS on SnO_2(110) is the HCOOH desorption step with an energy barrier of 0.36 eV (Figure 4b), agreeing with previous results in the literature.[29] Interestingly, on SnO_2/Ag(111), the *OCHO formation step with a lower free energy change of 0.22 eV becomes the PLS (Figure 4b), which is consistent with the improved CO_2-to-HCOOH conversion.

Further electronic structure calculations illustrate the binding modes of the key reaction intermediates on the active sites. The calculated local density of states (DOS) for *COOH on Ag(111) and SnO_2/Ag(111) are plotted in Figure 4c. The interactions between *COOH and Ag(111) are dominated by C−Ag binding (Figure 4c upper inset), giving rise to two C−Ag bonding states at −6.4 and −7.0 eV below the Fermi level. In the case of SnO_2/Ag(111), in addition to two C−Ag bonding states with lower energies at −6.7 and −7.3 eV, there are another two O−Sn bonding states at −6.7 and −8.7 eV, demonstrating strong O−Sn interactions between *COOH and the SnO_2 cluster (Figure 4c lower inset). The additional O−Sn binding contributed by the SnO_2 sites adds up to the thermodynamic stability of *COOH on the Ag sites and thus results in a lowered energy barrier for CO_2 reduction to CO on our SnO_x/Ag catalyst. For the HCOOH formation process, the local DOS of *OCHO are shown in Figure 4d. On SnO_2(110), two O−Sn bonding states at low energies of −9.1 and −10.7 eV suggest strong adsorption of *OCHO, which agrees well with the free energy profile in Figure 4b. For *OCHO on SnO_2/Ag(111), two bonding states of O1−Sn and O2−Ag exist at higher energies of −7.7 and −10.1 eV below the Fermi level (Figure 4d), indicating a weaker binding of the reaction intermediate on the SnO_2 sites with the direct participation of the neighboring Ag sites. The weakened adsorption of *OCHO facilitates HCOOH desorption and thus alters the PLS (Figure 4b).

To confirm the reliability of our DFT simulation study based on the SnO_2/Ag(111) model, we performed simulations with increased loadings of SnO_2 on the Ag surface. Compared to SnO_2/Ag(111), Sn_2O_4/Ag(111), and Sn_3O_6/Ag(111) show little difference in density of states (DOS) around the Fermi level energy (Figure S15), suggesting that the SnO_2 size has a

DOI: 10.1021/acsenergylett.8b01767
ACS Energy Lett. 2018, 3, 2816−2822

minimal impact on the electronic interactions and interfacial cooperation between Ag and SnO_2. To further verify the converging size effects, we calculated the free energy changes of CO_2 reduction on Sn_3O_6/Ag(111) and Sn_5O_{10}/Ag(111) based on the same approach used for SnO_2/Ag(111). The adsorption energies of the key reaction intermediates, *COOH and *OCHO, on Sn_3O_6/Ag(111) and Sn_5O_{10}/Ag(111) are reasonably close to the corresponding values on SnO_2/Ag(111) (Figure S16). In fact, the optimized geometries of the reaction intermediates adsorbed on these Sn_mO_n/Ag(111) surfaces are very similar (Figure S17).

To further rationalize the potential-dependent catalytic selectivity, we calculated the activation energy barriers for the PLS of the two CO_2 reduction reactions on SnO_2/Ag(111), taking into account the effects of the solvent.[44] The results can help determining the reaction free energies and activation energy barriers (Figure S18). The calculated activation energy barrier for the HCOOH pathway (1.46 eV) is significantly higher than that for the CO pathway (1.17 eV). As a consequence, at low overpotentials CO is the main product. However, at high overpotentials, when the energy barriers of both pathways can be overcome, the catalyst will preferentially produce HCOOH because of an energetically more favorable Gibbs free energy change for the formation of *OCHO (−0.41 eV) compared with that for *COOH (0.34 eV). Under working potentials of −0.6 V (for the CO pathway) and −1.0 V (for the HCOOH pathway), the transition state energy barriers are reduced to 0.65 and 0.78 eV, respectively (Figure S19), which are surmountable at room temperature.

For almost all CO_2-to-CO catalysts operating in aqueous electrolytes, H_2 evolution will start to dominate when the working electrode potential is negatively polarized beyond the CO production range. However, our SnO_x/Ag catalyst behaves differently: CO_2 reduction is switched to the HCOOH production mode and little H_2 is generated at more negative potentials. The origin of the suppression of H_2 evolution on the Ag sites is also understood by computational simulations where we find that the free energy change of atomic hydrogen adsorption (ΔG_{H^*}) on Ag(111) changes from 0.249 to 0.338 eV upon attaching a SnO_2 cluster to the Ag surface (Figure 4e). This ΔG_{H^*} change indicates even weaker *H adsorption on the Ag sites and thus makes H_2 evolution even more difficult. As a result, CO_2 conversion to HCOOH can proceed with a high FE. Because the SnO_2 sites do not directly participate in the binding of *H (Figure 4e), the reduced binding strength is mainly induced by the electronic interactions between Ag and SnO_2. This is understandable because electron donation to SnO_2 makes Ag(111) more positively charged and thus harder to adsorb H atoms. Our charge population calculations also support this argument with the result that *H on SnO_2/Ag(111) is less charged by 0.02 electrons than that on Ag(111) (Figure 4f).

In summary, this work discovers highly cooperative interactions at metal/oxide interfaces for electrocatalysis. The win-win metal−oxide cooperation enables both selective CO_2-to-CO conversion on the metal sites promoted by the oxide and selective CO_2-to-HCOOH conversion on the oxide sites promoted by the metal, on a single SnO_x/Ag heteronanostructured catalyst. The highly synergistic catalytic functionalities are attributed to the electronic interactions between the Ag and SnO_x components and their cooperative binding for specific key reaction intermediates at the interface, which optimize the kinetic barriers for both the CO_2 reduction and H_2 evolution reactions.

■ ASSOCIATED CONTENT

Supporting Information

The Supporting Information is available free of charge on the ACS Publications website at DOI: 10.1021/acsenergylett.8b01767.

Experimental and computational details, additional structural and electrochemical characterization results, and additional computational results (PDF)

■ AUTHOR INFORMATION

Corresponding Authors

*E-mail: hailiang.wang@yale.edu.
*E-mail: sunxm@mail.buct.edu.cn.
*E-mail: lcyin@imr.ac.cn.

ORCID

Zishan Wu: 0000-0003-4810-9112
Xiaoming Sun: 0000-0002-3831-6233
Hailiang Wang: 0000-0003-4409-2034

Notes

The authors declare no competing financial interest.

■ ACKNOWLEDGMENTS

This work is supported by the National Science Foundation (Grant CHE-1651717) and the Doctoral New Investigator grant from the ACS Petroleum Research Fund. X.S. thanks the National Science Fund of China (No. 51472249) for financial support. The theoretical calculations in this work were performed on TianHe-1(A) at National Supercomputer Center in Tianjing and Tianhe-2 at National Supercomputer Center in Guangzhou. L.Y. is also grateful to the Special Program for Applied Research on Super Computation of the NSFC-Guangdong Joint Fund (second phase) under Grant No. U1501501.

■ REFERENCES

(1) Roger, I.; Shipman, M. A.; Symes, M. D. Earth-Abundant Catalysts for Electrochemical and Photoelectrochemical Water Splitting. *Nat. Rev. Chem.* **2017**, *1* (1), 0003.

(2) Seh, Z. W.; Kibsgaard, J.; Dickens, C. F.; Chorkendorff, I.; Nørskov, J. K.; Jaramillo, T. F. Combining Theory and Experiment in Electrocatalysis: Insights into Materials Design. *Science* **2017**, *355* (6321), eaad4998.

(3) Sun, Y.; Gao, S.; Xie, Y. Atomically-Thick Two-Dimensional Crystals: Electronic Structure Regulation and Energy Device Construction. *Chem. Soc. Rev.* **2014**, *43* (2), 530−546.

(4) Wu, Y.; Wang, D.; Li, Y. Nanocrystals from Solutions: Catalysts. *Chem. Soc. Rev.* **2014**, *43* (7), 2112−2124.

(5) Li, Y.; Somorjai, G. A. Nanoscale Advances in Catalysis and Energy Applications. *Nano Lett.* **2010**, *10* (7), 2289−2295.

(6) Zhu, Y. P.; Guo, C.; Zheng, Y.; Qiao, S.-Z. Surface and Interface Engineering of Noble-Metal-Free Electrocatalysts for Efficient Energy Conversion Processes. *Acc. Chem. Res.* **2017**, *50* (4), 915−923.

(7) Kim, D.; Xie, C.; Becknell, N.; Yu, Y.; Karamad, M.; Chan, K.; Crumlin, E. J.; Nørskov, J. K.; Yang, P. Electrochemical Activation of CO_2 through Atomic Ordering Transformations of AuCu Nanoparticles. *J. Am. Chem. Soc.* **2017**, *139* (24), 8329−8336.

(8) Reske, R.; Mistry, H.; Behafarid, F.; Roldan Cuenya, B.; Strasser, P. Particle Size Effects in the Catalytic Electroreduction of CO_2 on Cu Nanoparticles. *J. Am. Chem. Soc.* **2014**, *136* (19), 6978−6986.

(9) Liu, M.; Pang, Y.; Zhang, B.; Luna, P. D.; Voznyy, O.; Xu, J.; Zheng, X.; Dinh, C. T.; Fan, F.; Cao, C.; García de Arquer, F. P.;

DOI: 10.1021/acsenergylett.8b01767
ACS Energy Lett. 2018, 3, 2816−2822

Safaei, T. S.; Mepham, A.; Klinkova, A.; Kumacheva, E.; Filleter, T.; Sinton, D.; Kelley, S. O.; Sargent, E. H. Enhanced Electrocatalytic CO_2 Reduction via Field-Induced Reagent Concentration. *Nature* **2016**, *537* (7620), 382.
(10) Mistry, H.; Reske, R.; Zeng, Z.; Zhao, Z.; Greeley, J.; Strasser, P.; Cuenya, B. R. Exceptional Size-Dependent Activity Enhancement in the Electroreduction of CO_2 over Au Nanoparticles. *J. Am. Chem. Soc.* **2014**, *136* (47), 16473−16476.
(11) Lin, S.; Diercks, C. S.; Zhang, Y. B.; Kornienko, N.; Nichols, E. M.; Zhao, Y.; Paris, A. R.; Kim, D.; Yang, P.; Yaghi, O. M.; Chang, C. J. Covalent Organic Frameworks Comprising Cobalt Porphyrins for Catalytic CO_2 Reduction in Water. *Science* **2015**, *349* (6253), 1208−1213.
(12) Cobo, S.; Heidkamp, J.; Jacques, P. A.; Fize, J.; Fourmond, V.; Guetaz, L.; Jousselme, B.; Ivanova, V.; Dau, H.; Palacin, S.; Fontecave, M.; Artero, V. A Janus Cobalt-Based Catalytic Material for Electro-Splitting of Water. *Nat. Mater.* **2012**, *11* (9), 802−807.
(13) Munnik, P.; de Jongh, P. E.; de Jong, K. P. Recent Developments in the Synthesis of Supported Catalysts. *Chem. Rev.* **2015**, *115* (14), 6687−6718.
(14) Deng, Y.; Cai, Y.; Sun, Z.; Liu, J.; Liu, C.; Wei, J.; Li, W.; Liu, C.; Wang, Y.; Zhao, D. Multifunctional Mesoporous Composite Microspheres with Well-Designed Nanostructure: A Highly Integrated Catalyst System. *J. Am. Chem. Soc.* **2010**, *132* (24), 8466−8473.
(15) Nørskov, J. K.; Bligaard, T.; Rossmeisl, J.; Christensen, C. H. Towards the Computational Design of Solid Catalysts. *Nat. Chem.* **2009**, *1* (1), 37−46.
(16) Zhang, Z.-C.; Xu, B.; Wang, X. Engineering Nanointerfaces for Nanocatalysis. *Chem. Soc. Rev.* **2014**, *43* (22), 7870−7886.
(17) Liu, W.; Hu, E.; Jiang, H.; Xiang, Y.; Weng, Z.; Li, M.; Fan, Q.; Yu, X.; Altman, E. I.; Wang, H. A Highly Active and Stable Hydrogen Evolution Catalyst Based on Pyrite-Structured Cobalt Phosphosulfide. *Nat. Commun.* **2016**, *7*, 10771.
(18) Weng, Z.; Jiang, J.; Wu, Y.; Wu, Z.; Guo, X.; Materna, K. L.; Liu, W.; Batista, V. S.; Brudvig, G. W.; Wang, H. Electrochemical CO_2 Reduction to Hydrocarbons on a Heterogeneous Molecular Cu Catalyst in Aqueous Solution. *J. Am. Chem. Soc.* **2016**, *138* (26), 8076−8079.
(19) Zhang, X.; Wu, Z.; Zhang, X.; Li, L.; Li, Y.; Xu, H.; Li, X.; Yu, X.; Zhang, Z.; Liang, Y.; Wang, H. Highly Selective and Active CO_2 Reduction Electrocatalysts Based on Cobalt Phthalocyanine/Carbon Nanotube Hybrid Structures. *Nat. Commun.* **2017**, *8*, 14675.
(20) Morales, F.; Weckhuysen, B. M. Promotion Effects in Co-based Fischer−Tropsch Catalysis. *Catalysis* **2006**, *19* (1), 1−40.
(21) Rodriguez, J. A.; Ma, S.; Liu, P.; Hrbek, J.; Evans, I.; Pérez, M. Activity of CeO_x and TiO_x Nanoparticles Grown on Au(111) in the Water-Gas Shift Reaction. *Science* **2007**, *318* (5857), 1757−1760.
(22) Behrens, M.; Studt, F.; Kasatkin, I.; Kühl, S.; Hävecker, M.; Abild-Pedersen, F.; Zander, S.; Girgsdies, F.; Kurr, P.; Kniep, B. L.; Tovar, M.; Fischer, R. W.; Nørskov, J. K.; Schlögl, R. The Active Site of Methanol Synthesis over $Cu/ZnO/Al_2O_3$ Industrial Catalysts. *Science* **2012**, *336*, 893.
(23) An, K.; Alayoglu, S.; Musselwhite, N.; Plamthottam, S.; Melaet, G.; Lindeman, A. E.; Somorjai, G. A. Enhanced CO Oxidation Rates at the Interface of Mesoporous Oxides and Pt Nanoparticles. *J. Am. Chem. Soc.* **2013**, *135* (44), 16689−16696.
(24) Strmcnik, D.; Uchimura, M.; Wang, C.; Subbaraman, R.; Danilovic, N.; Vliet, D. V. D.; Paulikas, A. P.; Stamenkovic, V. R.; Markovic, N. M. Improving the Hydrogen Oxidation Reaction Rate by Promotion of Hydroxyl Adsorption. *Nat. Chem.* **2013**, *5* (4), 300−306.
(25) Wang, C.; Daimon, H.; Sun, S. Dumbbell-Like $Pt-Fe_3O_4$ Nanoparticles and Their Enhanced Catalysis for Oxygen Reduction Reaction. *Nano Lett.* **2009**, *9* (4), 1493−1496.
(26) Weng, Z.; Liu, W.; Yin, L. C.; Fang, R.; Li, M.; Altman, E. I.; Fan, Q.; Li, F.; Cheng, H. M.; Wang, H. Metal/Oxide Interface Nanostructures Generated by Surface Segregation for Electrocatalysis. *Nano Lett.* **2015**, *15* (11), 7704−7710.
(27) Gao, S.; Lin, Y.; Jiao, X.; Sun, Y.; Luo, Q.; Zhang, W.; Li, D.; Yang, J.; Xie, Y. Partially Oxidized Atomic Cobalt Layers for Carbon Dioxide Electroreduction to Liquid Fuel. *Nature* **2016**, *529* (7584), 68−71.
(28) Luc, W.; Collins, C.; Wang, S.; Xin, H.; He, K.; Kang, Y.; Jiao, F. Ag-Sn Bimetallic Catalyst with a Core-Shell Structure for CO_2 Reduction. *J. Am. Chem. Soc.* **2017**, *139* (5), 1885−1893.
(29) Li, Q.; Fu, J.; Zhu, W.; Chen, Z.; Shen, B.; Wu, L.; Xi, Z.; Wang, T.; Lu, G.; Zhu, J. J.; Sun, S. Tuning Sn-Catalysis for Electrochemical Reduction of CO_2 to CO via the Core/Shell Cu/SnO_2 Structure. *J. Am. Chem. Soc.* **2017**, *139* (12), 4290−4293.
(30) Huo, S.; Weng, Z.; Wu, Z.; Zhong, Y.; Wu, Y.; Fang, J.; Wang, H. Coupled Metal/Oxide Catalysts with Tunable Product Selectivity for Electrocatalytic CO_2 Reduction. *ACS Appl. Mater. Interfaces* **2017**, *9* (34), 28519−28526.
(31) Larrazábal, G. O.; Martín, A. J.; Mitchell, S.; Hauert, R.; Pérez-Ramírez, J. Enhanced Reduction of CO_2 to CO over Cu-In Electrocatalysts: Catalyst Evolution Is the Key. *ACS Catal.* **2016**, *6* (9), 6265−6274.
(32) Gao, D.; Zhang, Y.; Zhou, Z.; Cai, F.; Zhao, X.; Huang, W.; Li, Y.; Zhu, J.; Liu, P.; Yang, F.; Wang, G.; Bao, X. Enhancing CO_2 Electroreduction with the Metal-Oxide Interface. *J. Am. Chem. Soc.* **2017**, *139* (16), 5652−5655.
(33) Schreier, M.; Héroguel, F.; Steier, L.; Ahmad, S.; Luterbacher, J. S.; Mayer, M. T.; Luo, J.; Grätzel, M. Solar Conversion of CO_2 to CO Using Earth-Abundant Electrocatalysts Prepared by Atomic Layer Modification of CuO. *Nat. Energy* **2017**, *2* (7), 17087.
(34) Ghoshtagore, R. Mechanism of CVD Thin Film SnO_2 Formation. *J. Electrochem. Soc.* **1978**, *125* (1), 110−117.
(35) Rai, P.; Majhi, S. M.; Yu, Y.-T.; Lee, J.-H. Synthesis of Plasmonic $Ag@SnO_2$ Core-Shell Nanoreactors for Xylene Detection. *RSC Adv.* **2015**, *5* (23), 17653−17659.
(36) Kim, C.; Jeon, H. S.; Eom, T.; Jee, M. S.; Kim, H.; Friend, C. M.; Min, B. K.; Hwang, Y. J. Achieving Selective and Efficient Electrocatalytic Activity for CO_2 Reduction Using Immobilized Silver Nanoparticles. *J. Am. Chem. Soc.* **2015**, *137* (43), 13844−13850.
(37) Zhang, S.; Kang, P.; Meyer, T. J. Nanostructured Tin Catalysts for Selective Electrochemical Reduction of Carbon Dioxide to Formate. *J. Am. Chem. Soc.* **2014**, *136* (5), 1734−1737.
(38) Li, X.; Liu, W.; Zhang, M.; Zhong, Y.; Weng, Z.; Mi, Y.; Zhou, Y.; Li, M.; Cha, J. J.; Tang, Z.; Jiang, H.; Li, X.; Wang, H. Strong Metal-Phosphide Interactions in Core-Shell Geometry for Enhanced Electrocatalysis. *Nano Lett.* **2017**, *17* (3), 2057−2063.
(39) Gao, D.; Zhou, H.; Cai, F.; Wang, D.; Hu, T.; Jiang, B.; Cai, W. B.; Chen, X.; Si, R.; Yang, F.; Miao, S.; Wang, J.; Wang, G.; Bao, X. Switchable CO_2 Electroreduction via Engineering Active Phases of Pd Nanoparticles. *Nano Res.* **2017**, *10* (6), 2181−2191.
(40) Min, X. Q.; Kanan, M. W. Pd-Catalyzed Electrohydrogenation of Carbon Dioxide to Formate: High Mass Activity at Low Overpotential and Identification of the Deactivation Pathway. *J. Am. Chem. Soc.* **2015**, *137* (14), 4701−4708.
(41) Maity, K.; Panda, D. K.; Lochner, E.; Saha, S. Fluoride-Induced Reduction of Ag(I) Cation Leading to Formation of Silver Mirrors and Luminescent Ag-Nanoparticles. *J. Am. Chem. Soc.* **2015**, *137* (8), 2812−2815.
(42) Gaarenstroom, S. W.; Winograd, N. Initial and Final State Effects in the ESCA Spectra of Cadmium and Silver Oxides. *J. Chem. Phys.* **1977**, *67* (8), 3500−3506.
(43) Rosen, J.; Hutchings, G. S.; Lu, Q.; Rivera, S.; Zhou, Y.; Vlachos, D. G.; Jiao, F. Mechanistic Insights into the Electrochemical Reduction of CO_2 to CO on Nanostructured Ag Surfaces. *ACS Catal.* **2015**, *5* (7), 4293−4299.
(44) Seifitokaldani, A.; Gabardo, C. M.; Burdyny, T.; Dinh, C.-T.; Edwards, J. P.; Kibria, M. G.; Bushuyev, O. S.; Kelley, S. O.; Sinton, D.; Sargent, E. H. Hydronium-Induced Switching between CO_2 Electroreduction Pathways. *J. Am. Chem. Soc.* **2018**, *140* (11), 3833−3837.

DOI: 10.1021/acsenergylett.8b01767
ACS Energy Lett. 2018, 3, 2816−2822